Supporting Information for

One-Electron Oxidation of an Oxoiron(IV) Complex to Form an $[O=Fe^{V}=NR]^{+}$ Center

Katherine M. Van Heuvelen,[a,b] Adam T. Fiedler[a,b] Xiaopeng Shan,[a,b] Raymond F. De Hont,[c] Katlyn K. Meier,[c] Emile L. Bominaar,[c] Eckard Münck,[c] and Lawrence Que, Jr.[a,b]

[a]Department of Chemistry and [b]Center for Metals in Biocatalysis, University of Minnesota, Minneapolis, MN 55455, and [c]Department of Chemistry, Carnegie Mellon University, Pittsburgh, PA 15213.

Table S1. Mulliken spin populations P(X), idealized valence state formulation, ^{57}Fe isomer shifts, quadrupole splitting, and asymmetry parameter from DFT.

Table S2. Magnetic hyperfine coupling constants (in MHz, Fermi contact plus spin dipolar) deduced from DFT using for each complex the model suggested by **Table S1.**

Table S3. Section of **Table S2** but using the experimental A_{iso} (^{57}Fe) value instead of the calculated Fermi contact term

Table S4. $A_{x,y,z}$-values (in MHz, Fermi contact + spin dipolar) from experiment compared with results deduced from DFT with Fe^{IV}-radical model and Fe^{V} model (shaded) for **2**, and two hypothetical complexes containing Fe^{IV}-radical ($Fe^{IV}N\bullet$) and Fe^{V} sites.

Table S5. Fe-O stretch frequencies and axial bond lengths from DFT.

Table S6. A-values (in MHz, Fermi contact plus spin dipolar) deduced from DFT using Fe^{IV}-Radical model and Fe-N_{ax} distances (in Å) from relaxed B3LYP/6-311G scan along Fe-O_{ax}

Table S7. Mulliken spin (first row) and total (second row) populations of 3d orbitals at Fe and 2p orbitals at N and O_{ax}, for the Fe^{V} $|d_{x2-y2}^{2}\ d_{yz}^{1}|$ BP86 solution for the N-proximal conformation of **2**. Axes: z is along N-Fe-O_{ax} bonds and x is here the intersection of TMC-nitrogen plane and acetamide NCO plane.

Figure S1. 3d-type molecular orbitals of the Fe^{V} $|d_{x2-y2}^{2}\ d_{yz}^{1}|$ BP86 solution for **2**.

Figure S2. Spin density contour plots of **2,** $\boldsymbol{1_{ox}}$, and the truncated TAML complex $[Fe^{V}(O)B^{*}]^{1-}$

Figure S3. Plot of spin density in acetamidyl radical obtained with BP86.

Figure S4. 4.2 K/8.0 T Mössbauer spectrum of the sample containing **2-H**$^{+}$ (Sample from Figure 3C).

Figure S5. 40 K EPR spectrum of **2**.

Figure S6. X-band EPR spectrum of ^{17}O labeled

Figure S7. rR spectra of samples of **2** prepared with ^{16}O, ^{17}O, and ^{18}O.

Figure S8. ESI-MS spectra of **2** along with theoretical isotope distribution patterns associated with $\mathbf{2_N}$.

Figure S9. ESI-MS spectra of **2** prepared in 3:1 CH_2Cl_2:CH_3CN (left) and 3:1 CH_2Cl_2:CD_3CN.

DFT Calculations

The DFT calculations presented in **Tables S1-S7** and **Figures S1-S3** were performed Gaussian '09, Revision B.01, M. J. Frisch, G. W. Trucks, H. B. Schlegel, G. E. Scuseria, M. A. Robb, J. R. Cheeseman, G. Scalmani, V. Barone, B. Mennucci, G. A. Petersson, H. Nakatsuji, M. Caricato, X. Li, H. P. Hratchian, A. F. Izmaylov, J. Bloino, G. Zheng, J. L. Sonnenberg, M. Hada, M. Ehara, K. Toyota, R. Fukuda, J. Hasegawa, M. Ishida, T. Nakajima, Y. Honda, O. Kitao, H. Nakai, T. Vreven, J. A. Montgomery, Jr., J. E. Peralta, F. Ogliaro, M. Bearpark, J. J. Heyd, E. Brothers, K. N. Kudin, V. N. Staroverov, T. Keith, R. Kobayashi, J. Normand, K. Raghavachari, A. Rendell, J. C. Burant, S. S. Iyengar, J. Tomasi, M. Cossi, N. Rega, J. M. Millam, M. Klene, J. E. Knox, J. B. Cross, V. Bakken, C. Adamo, J. Jaramillo, R. Gomperts, R. E. Stratmann, O. Yazyev, A. J. Austin, R. Cammi, C. Pomelli, J. W. Ochterski, R. L. Martin, K. Morokuma, V. G. Zakrzewski, G. A. Voth, P. Salvador, J. J. Dannenberg, S. Dapprich, A. D. Daniels, O. Farkas, J. B. Foresman, J. V. Ortiz, J. Cioslowski, D. J. Fox, Gaussian, Inc., Wallingford CT, 2010.

Table S1. Mulliken spin populations P(X), idealized valence state formulation, ^{57}Fe isomer shifts, quadrupole splitting, and asymmetry parameter from DFT

functional	Complex	P(Fe)	P(^{17}O)	P(N_{am})	Formulation [e]	δ (mm/s)	ΔE_Q [d] (mm/s)	η
B3LYP [a]	**2**	1.34	0.70	-0.85	$Fe^{IV}N\bullet$	0.14	-0.48	0.75
B3LYP [a]	**2-H$^+$**	1.25	0.79	-0.92	$Fe^{IV}N\bullet$	0.13	0.52	0.66
B3LYP [b]	**1**	1.34	0.79	−	Fe^{IV}	0.18	1.17	0.09
B3LYP [c]	**1_{ox}**	0.35	0.65	−	$Fe^{IV}O\bullet$	-0.09	2.83	0.93
BP86 [a]	**2**	0.86	0.51	-0.30	Fe^{V}	0.03	1.08	0.47
BP86 [a]	**2-H$^+$**	0.77	0.55	-0.31	Fe^{V}	-0.05	-1.17	0.48
BP86 [b]	**1**	1.30	0.76	−	Fe^{IV}	0.16	1.08	0.17
BP86 [c]	**1_{ox}**	0.90	0.27	−	Fe^{V}	-0.08	2.52	0.92

[a] $[Fe(O)(NC(Me)O(H))(TMC)]^{1+(2+)}$. [b] Fe^{IV}(O)(NCMe)(TMC). [c] Fe^{V}(O)(NCMe)(TMC). [d] Used Q(^{57}Fe) = 0.16 barn. [e] Based on spin populations and $\langle \mathbf{S}^2 \rangle$ values.

The spin populations calculated for **2** and **2-H$^+$** are given in **Table S1** and show that hybrid functional B3LYP yields solutions that are best described as iron(IV)-radical, $Fe^{IV}N\bullet$, species, while the BP86 solutions are best described as Fe^{V}. The difference in the performance of B3LYP and BP86 in predicting the valencies of the atoms in these systems is probably rooted in their respectively "hybrid" and "pure" natures (the pure functionals PBEVWN and OLYP gave similar results as BP86). The functional dependence of the results may be related to the propensity of Hartree-Fock exchange toward stabilizing high-spin states. Applied to the present situation, the HF-exchange contribution included in the B3LYP functional explains why this functional favors the $Fe^{IV}N\bullet$ formulation (three unpaired electrons of which two are on iron) over the Fe^{V} formulation (one unpaired electron). The Fe^{IV}-radical state for B3LYP and the Fe^{V} state for BP86 are strongly supported by the expectation values $\langle \Psi_{B3LYP}|\mathbf{S}^2|\Psi_{B3LYP}\rangle = 1.63$ (ideally 1¾ for the broken symmetry state of the Fe^{IV}-radical model) and $\langle \Psi_{BP86}|\mathbf{S}^2|\Psi_{BP86}\rangle = 0.94$ (ideally ¾ for the Fe^{V} model).

The isomer shift, δ, and quadrupole splitting, ΔE_Q, have no clear preference for any of the two functionals. The solutions with Fe^{IV}-radical character (B3LYP solutions) give isomer shifts that are higher than the observed value (δ_{exp} = 0.10 (4) mm/s) while those with Fe^{V} character, all

obtained with BP86, are somewhat lower than in experiment. The quadrupole splittings for B3LYP are in slightly better agreement with experiment than those for BP86 but the discrepancies for the latter functional are also within the commonly observed error margin for this quantity (±0.5 mm/s). Also included in **Table S1** are the results for the starting material **1** (Fe^{IV}=O) and its hypothetical 1-electron oxidized adduct $\mathbf{1_{ox}}$ (Fe^{V}=O). The isomer shifts for **2** and **2-H**$^+$ with Fe^{IV}-radical character are consistent with the isomer shift of the Fe^{IV}=O starting material. The isomer shift calculated for the Fe^{V} solution of **2** (δ = +0.03 mm/s) is considerably larger than computed for the hypothetical Fe^{V}(O)(NCMe)(TMC) complex $\mathbf{1_{ox}}$ (δ = -0.08 mm/s), in spite of having rather similar spin populations. Apparently, the replacement of the acetonitrile ligand in $\mathbf{1_{ox}}$ with an acetimido ligand, gives rise to a significant increase in the isomer shifts, even if the oxidation state remains Fe^{V}, as in the BP86 solution for **2**. Thus, as it has already been noted earlier in the literature, the isomer shift is a poor indicator of iron valence state unless the ligand effect on this quantity is properly accounted for. The difference of the δ values for **2** (δ = 0.03 mm/s) and experiment (δ = 0.10 mm/s) is within the standard error of the BP86 isomer shift calibration ($\Delta\delta$ = 0.09 mm/s). The negative change in the isomer shift observed upon protonation (**2-H**$^+$) has the sign expected for the anticipated increase in Fe^{V} character but is not unambiguously supported by the data. The quadrupole splittings obtained with the two functionals for $\mathbf{1_{ox}}$ are significantly larger (~2.5 mm/s) than observed in **2** and **2-H**$^+$ by Mössbauer ($\Delta E_{Q,exp}$ ~ 0.50 mm/s). This observation does not preclude Fe^{V} as iron valence state in **2** and **2-H**$^+$, because the BP86 states for **2** and **2-H**$^+$, while clearly Fe^{V} on the basis of spin density and $\langle \mathbf{S}^2 \rangle$, have dramatically smaller values for ΔE_Q (~ 1 mm/s vs. 2.5 mm/s in $\mathbf{1_{ox}}$). This difference shows that quadrupole splitting ΔE_Q, like isomer shift δ, is sometimes an ambiguous reporter for the iron oxidation state because of its ligand dependence. DFT supports this assessment: the replacement of acetonitrile with the redox labile acetimido nitrogen *trans* to the oxo ligands gives a large change in the calculated values for ΔE_Q.

The *Fe^{IV}-radical* solutions for **2** and **2-H**$^+$ obtained with B3LYP and the *Fe^{V}* solutions obtained with BP86 require different treatments of the magnetic hyperfine interactions. In the Fe^{IV}-radical formulation, the magnetic hyperfine interaction of ^{14}N nucleus arises from the magnetic coupling of this nucleus with a π radical electron centered at this nucleus, $\mathbf{S}_R \cdot a_R \cdot \mathbf{I}_R$. The radical spin is coupled to the S_{Fe}=1 spin of the iron to give a total spin S=1/2, introducing spin projection factors of 4/3 (Fe^{IV}, S_{Fe}=1) and -1/3 (N•, S_R=1/2) in the expression for the magnetic hyperfine coupling constants in the coupled S = 1/2 representation. In order to express the DFT calculated quantities with those obtained by analyzing the data with an S = ½ spin Hamiltonian, the DFT quantities have to be expressed in the coupled representation: $\mathbf{S} \cdot A_X \cdot \mathbf{I}_X$ (X = Fe, N, O) where **S** is the coupled S=1/2 system spin, $|\{S_{Fe}=1, S_R=1/2\}S=1/2\rangle$. For the ^{57}Fe and the ^{17}O of the oxo group, the DFT output for the A-tensors has to be dived by 2 (to refer the values to the S_{Fe}=1 Hamiltonian) and then multiplied by the spin projection factor 4/3. For ^{14}N the signs of the a_R values have to be reversed (it is a β spin) and then multiplied by spin projection factor -1/3. This yields the entries in rows 1-4 of **Table S2** which allows direct comparison between the calculated and experimental A-values. Note that the calculated ^{57}Fe A-tensors are quite axial around z, in contrast to the experimental data.

In the Fe^{V} model the DFT calculated A-tensors can be directly compared with the experimental A-tensors. For a final comparison we wish to make one adjustment. It is well known that DFT often underestimates the magnitude of the Fermi contact interaction, A_{FC}, and researchers have either introduced correction factors (as much as 1.7) or used the experimentally determined contact term. Since the g-values of **2** and **2-H**$^+$ are close to g = 2, orbital

contributions to the A-tensor are negligible, and thus we can use $A_{iso} = (A_x + A_y + A_z)/3$ for A_{FC}. Using the experimental value A_{iso} (^{57}Fe) = (- 48 - 17 + 0)/3 MHz = -21.7 MHz for **2** and **2-H$^+$** further improves an already excellent agreement with experiment as can be seen by inspection of **Table S3**.

Table S2. Magnetic hyperfine coupling constants (in MHz, Fermi contact + spin dipolar) deduced from DFT using for each complex the model suggested by **Table S1**

functional	Complex	State [b]	^{57}Fe			$^{14}N_{ax}$			^{17}O		
			A_x	A_y	A_z	A_x	A_y	A_z	A_x	A_y	A_z
B3LYP [a]	**2**	$Fe^{IV}N\bullet$	-24.7	-27.5	6.3	-32.7	2.2	3.3	-56.1	-57.0	54.4
B3LYP [a]	**2-H$^+$**	$Fe^{IV}N\bullet$	-24.2	-19.2	4.8	-35.6	-0.9	3.2	-57.9	-62.5	63.1
BP86 [a,c]	**2**	Fe^{V}	**-35.5**	**-10.7**	**4.5**	**-39.3**	**10.8**	**6.1**	**-1.0**	**-70.8**	**75.7**
BP86 [a,c]	**2-H$^+$**	Fe^{V}	**-35.5**	**-4.4**	**3.6**	**-35.5**	**-1.2**	**3.9**	**18.4**	**-91.4**	**84.7**
exp	**2**, **2-H$^+$**		-48	-17	0	29	11	11	30	133	20

[a] $[Fe(O)(NC(Me)O(H))(TMC)]^{1+(2+)}$. [b] State used for interpreting DFT results for magnetic hyperfine interactions (cf. **Table S1**). [c] Rows having most satisfactory agreement with experimental data for **2** and **2-H$^+$** are in bold face.

None of the computed A-value sets listed for the $Fe^{IV}N\bullet$ state (**Table S2**) gives a satisfactory agreement with experiment. The A-values obtained for ^{57}Fe and ^{17}O in the $Fe^{IV}N\bullet$ state are nearly axial along z and not rhombic (^{57}Fe) or quasi axial along y (^{17}O) as observed. The experimental magnetic hyperfine data for ^{14}N, ^{57}Fe, and ^{17}O for **2** and **2-H$^+$** reveal A-values with a characteristic set of spatially correlated anisotropies. The A tensor for $^{14}N_{ax}$ has one large and two small components. Let us define the direction with the large $^{14}N_{ax}$ A-component as the x axis. The A values for both ^{57}Fe and ^{17}O show marked anisotropies. ^{57}Fe has one large, one intermediate, and one vanishing A-component. The largest component of A(Fe) is along x and we define the eigenvector of the intermediate component as the y axis (this choice of axes assigns the vanishing component to the z axis, as in Fe^{IV}(O)(TMC)(NCMe) (-25 T, -20 T, -3 T) where z is along the Fe-O bond. $^{17}O_{ax}$ has one large and two smaller A-components, with the large component being along the y axis. B3LYP consistently fails to reproduce the anisotropies of both the ^{57}Fe and ^{17}O A-values (**Table S2**). This property is anticipated from **Table S1**, which shows that the spin densities calculated with B3LYP for the Fe=O unit in **2** and **2-H$^+$** are similar to those for starting complex **1**, and share with them nearly z-axial A-values. Clearly, there is no Fe^{IV} solution for **2** and **2-H$^+$**. The best agreement with the experimental results is obtained for the Fe^{V} state predicted by BP86 for **2** and **2-H$^+$** (bold faced rows of **Table S2**), which have similar A values.

Table S3. Section of **Table S2** but using the experimental A_{iso} (^{57}Fe) value instead of the calculated Fermi contact term

functional	Complex	State	^{57}Fe			$^{14}N_{imido}$			^{17}O		
			A_x	A_y	A_z	A_x	A_y	A_z	A_x	A_y	A_z
BP86	**2**	Fe^{V}	**-43.3**	**-18.5**	**3.3**	**-39.3**	**10.8**	**6.1**	**-1.0**	**-70.8**	**75.7**
BP86	**2-H$^+$**	Fe^{V}	**-45.1**	**-14.0**	**-6.0**	**-35.5**	**-1.2**	**3.9**	**18.4**	**-91.4**	**84.7**
exp	**2**, **2-H$^+$**		-48	-17	0	29	11	11	30	133	20

Table S4. $A_{x,y,z}$-values (in MHz, Fermi contact + spin dipolar) from experiment compared with results deduced from DFT with Fe^{IV}-radical model and Fe^{V} model (shaded) for **2**, and two hypothetical complexes containing Fe^{IV}-radical ($Fe^{IV}N\bullet$) and Fe^{V} sites

Nucleus	Axis	Exp	B3LYP				BP86			
			2 [c]	*2($Fe^{IV}N\bullet$)* [a]	**2** [f]	*2(Fe^{V})* [b,d]	**2** [c]	*2($Fe^{IV}N\bullet$)* [a]	**2** [d,f]	*2(Fe^{V})* [b,d]
^{57}Fe	x	-48	-24.7	-27.1	N.A.[g]	**-46.4**	N.A.[h]	-23.7	**-35.5**	**-40.0**
	y	-17	-27.5	-26.5		**16.0**		-25.3	**-10.7**	**-4.7**
	z[e]	0	6.3	2.4		**-1.1**		1.7	**4.5**	**3.3**
^{17}O	x	30	-56.1	-60.2		**-27.9**		-36.9	**-1.0**	**78.7**
	y	133	-57.0	-60.3		**-100.5**		-35.7	**-70.8**	**-118.3**
	z[e]	20	54.4	65.0		**75.9**		81.0	**75.7**	**47.4**

[a] A-values obtained on the basis of the A(^{57}Fe) and A(^{17}O) calculated for a hypothetical system in which an Fe^{IV}=O (S_{Fe}=1) site as in **1** is coupled to a (amidyl) radical (S_R=1/2) to give total spin S=½. [b] A-values for $\mathbf{1_{ox}}$. [c] A-values for **2** obtained with Fe^{IV}-radical model in coupled representation. [d] Columns showing data resembling the experimental data for **2** and **2-H$^+$** are in bold face. [e] z is along the Fe-^{17}O vector. [f] A-values obtained with Fe^{V} model. [g] Fe^{V} model not applicable. [h] Fe^{IV}-radical model not applicable

Observations from **Table S4**: (i) B3LYP and BP86 give for the iron site in the hypothetical $Fe^{IV}N\bullet$ complex similar A-values. (ii) B3LYP and BP86 give for the iron(V) site in $\mathbf{1_{ox}}$ similar A values. (iii) The corresponding differences between the A-values for ^{17}O are somewhat larger than for iron. (iv) B3LYP and BP86 give for $Fe^{IV}N\bullet$ axial ^{57}Fe and ^{17}O A-values. (v) B3LYP and BP86 give ^{57}Fe and ^{17}O A-values for $\mathbf{1_{ox}}$ that show similar spatial anisotropies. (vi) B3LYP gives essentially the same results for **2** and $Fe^{IV}N\bullet$. This observation shows that the Fe site in the B3LYP solution of **2** is best described as an Fe^{IV}-radical system (this conclusion is supported by the spin populations obtained with B3LYP given in **Table S1**). (vii) BP86 gives excellent agreement between **2** and Fe^{V}. This observation shows that the Fe site in the BP86 state for **2** is best described as Fe^{V} (this conclusion is supported by the spin populations obtained with BP86 given in **Table S1**). Thus, the difference between B3LYP and BP86 is not so much in the calculation of the properties *per se* but in the balance between the Fe^{IV}-radical and Fe^{V} configurations, which is tipped toward Fe^{IV}-radical by B3LYP and toward Fe^{V} by BP86 (see discussion below **Table S1**). (viii) *The B3LYP results for **2** are in poor agreement with experiment*; in particular, they fail to reproduce the anisotropic A tensors observed. The reason for this shortcoming is that the B3LYP solution for **2** is an Fe^{IV}-radical state in which the Fe^{IV}=O moiety retains the axial features of starting complex **1**. (ix) The BP86 results for **2** are in good agreement with experiment; in particular, they reproduce the rhombic A tensors (the agreement for iron is excellent; for ^{17}O the agreement is fine, except for a discrepancy in the z component). The reason for the improved agreement is that the BP86 solution for **2** has predominant Fe^{V} character. (NB. If B3LYP is forced into the Fe^{V} state, as in the calculation for $\mathbf{1_{ox}}$, a similarly good agreement is found for this functional as well). The A-values are explained on the basis of the Fe^{V} formulation in the discussion of **Figure 5** of main text.

Table S5. Fe-O stretch frequencies and axial bond lengths from DFT

functional	Complex	State	ν_{Fe-O} (cm^{-1})	Fe-^{17}O (Å)	Fe-N_{ax} (Å)
B3LYP [a]	**2**	$Fe^{IV}N\bullet$	855	1.669	1.905
B3LYP [a]	**2-H$^+$**	$Fe^{IV}N\bullet$	898	1.642	1.985
B3LYP [b]	**1**	Fe^{IV}	910	1.641	2.097
B3LYP [c]	$\mathbf{1_{ox}}$	Fe^{V}	1256	1.584	2.022
BP86 [a]	**2**	Fe^{V}	**785** [d]	1.701	1.781
BP86 [a]	**2-H$^+$**	Fe^{V}	**829** [d]	1.658	1.813
BP86 [b]	**1**	Fe^{IV}	**853** [d]	1.664	2.037
BP86 [c]	$\mathbf{1_{ox}}$	Fe^{V}	944	1.603	2.006

[a] $[Fe(O)(NC(Me)O(H))(TMC)]^{1+(2+)}$. [b] $Fe^{IV}(O)(NCMe)(TMC)$. [c] $Fe^{V}(O)(NCMe)(TMC)$. [d] Numbers having most satisfactory agreement with the experimental data for **2**, **2-H$^+$** and **1** are in bold face.

Table S5 shows that B3LYP gives consistently stronger the Fe-^{17}O bonds than BP86 for all complexes listed, resulting in shorter bond lengths and higher Fe-O stretch frequencies for the former functional. The Fe-O stretch frequencies obtained with BP86 are in better agreement with experiment than those calculated with B3LYP, which are significantly higher than observed. Both functionals reproduce the increasing trend in the experimental Fe-O frequencies for **2**, **2-H$^+$** and **1**: 798 cm^{-1} < 811 cm^{-1} < 839 cm^{-1}. Irrespective of the functional used, the frequencies calculated for **2** and **2-H$^+$** are considerably smaller than for the Fe^{IV}=O bond in **1** and the Fe^{V}=O bond in $\mathbf{1_{ox}}$, suggesting the Fe-O stretch frequency to be a poor reporter for the oxidation state of iron in the present case where iron is coordinated by a redox labile imido *trans* to the oxo ligand. The induced weakening of the Fe-O bond correlates with the increase in isomer shift (see main text).

Table S6. $A_{x,y,z}$-values (in MHz, Fermi contact + spin dipolar) deduced from DFT using Fe^{IV}-Radical model and Fe-N_{ax} distances (in Å) from relaxed B3LYP/6-311G scan along Fe-O_{ax}

Fe-O_{ax} [a]	Fe-N	^{57}Fe [b]			^{57}Fe [c]			^{14}N			^{17}O		
		x	y	z	x	y	z	x	y	z	x	y	z
1.669 [d]	1.904	-17.1	-12.3	29.4	-24.7	-21.5	6.3	-71.0	33.7	37.3	-54.5	-56.4	110.9
1.699	1.897	-17.0	-12.1	29.1	-24.6	-21.3	6.1	-70.7	33.7	37.0	-54.9	-56.7	111.6
1.729	1.891	-17.0	-11.9	28.9	-24.5	-21.1	6.1	-70.6	33.8	36.8	-55.2	-57.1	112.3
1.759	1.884	-16.9	-11.6	28.5	-24.4	-20.9	5.9	-70.4	33.9	36.5	-55.4	-57.6	113.0
1.789	1.878	-16.8	-11.3	28.1	-24.2	-20.5	5.7	-70.2	34.0	36.2	-55.2	-58.6	113.8
1.819	1.871	-17.0	-10.6	27.6	-24.2	-19.9	5.5	-70.1	34.2	35.9	-61.8	-53.0	114.8

[a] Value of imposed distance in optimization.
[b] Using for ^{57}Fe a^{FC} = -16.25 MHz ($\mathbf{I}\cdot a^{FC}\cdot\mathbf{S}_{Fe}$, S_{Fe} = 1), the value obtained from the average of the experimental A values by multiplication with 3/4.
[c] Using the DFT calculated A^{FC}.
[d] Distance in the B3LYP/6-311G optimized structure; other distances of relaxed scan are defined by incrementing five times by 0.03 Å.

The DFT-functional dependence of the bond distances raises the possibility that the differences in the performance of the functionals in the A-value calculations arise from differences in the bond distances in the optimized geometries obtained with these functionals. In **Table S6** we have listed the results for the A-values from a relaxed B3LYP/6-311G scan along the Fe-^{17}O coordinate. The changes in the A-values appear to be remarkably small given the broad range of Fe-O distances considered. A similar insensitivity of the A-values is observed in a relaxed scan along the Fe-N_{ax} coordinate. These results together with the insensitivity of the A-values to basis set changes (we used 6-311G, 6-311G*, TZVP) corroborate with the conclusion that the computational differences between the A values obtained with B3LYP versus BP86 and two other pure functionals (PBEVWN and OLYP) are rooted in the type of solution obtained with these functionals (see discussion below **Table S1**).

Table S7. Mulliken spin (first row) and total (second row) populations of 3d orbitals at Fe and 2p orbitals at N_{ax} and O_{ax}, for the Fe^V $|d_{x2-y2}^2\ d_{yz}^1|$ BP86 solution for **2**. Axes: z is along N-Fe-O_{ax} bonds and x is here the intersection of TMC-nitrogen plane and acetamide NCO plane.[a]

Fe					N_{ax}			O_{ax}		
x^2-y^2	xz [b]	yz [c]	xy	z^2	x	y	z	x	y	z
0.01	0.23	**0.53**	0.06	0.02	**-0.30**	0.03	-0.02	0.18 [d]	**0.32**	0.01
1.82 [e]	1.21	1.42	0.82 [e]	0.94	1.19	1.45	1.20	1.55	1.59	1.41

[a] Dominant spin densities are given in bold face.
[b] α spin population = 0.71, β spin population 0.49.
[c] α spin population = 0.97, β spin population 0.44.
[d] This number is not zero because the donation of electron density into the formally empty d_{xz} orbital is not completely spin balanced due to the presence of the α spin electron in d_{yz}.
[e] These values approach 2.0 and 0.6 by rotating x and y slightly around z as to make x and y more accurately bisect the equatorial N-Fe-N angles.

The spin and total populations for the BP86 solution for **2** concur with earlier DFT studies in that the formally empty metal d orbitals in high-valent iron complexes acquire large electronic populations due to covalent interactions with the ligands.

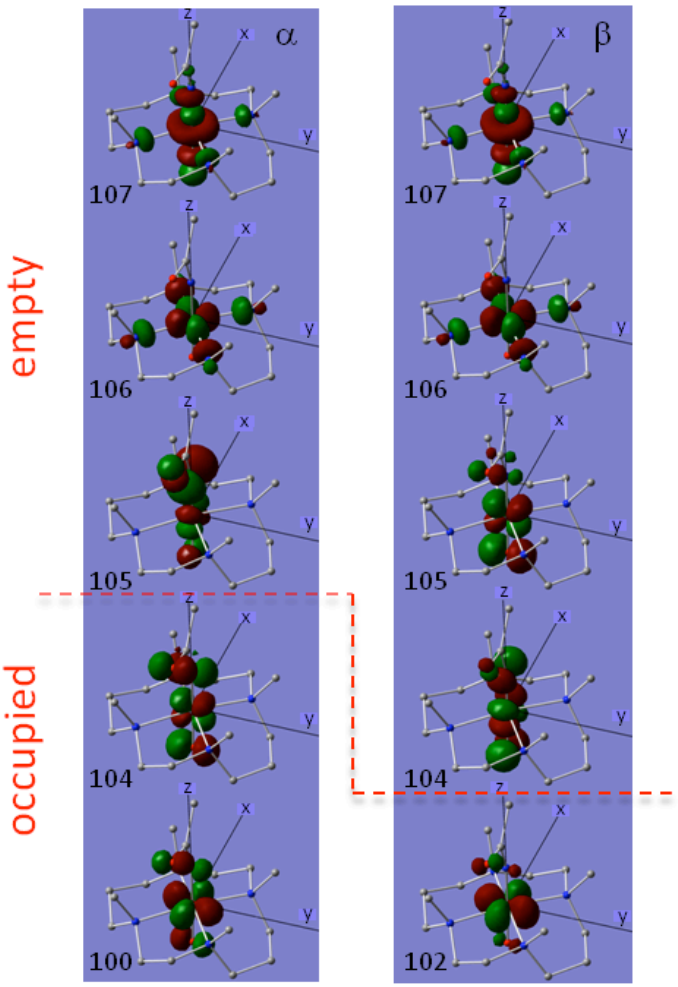

Figure S1. 3d-type molecular orbitals of the Fe^{V} $|d_{x2-y2}^{2}\ d_{yz}^{1}|$ BP86 solution for **2**.

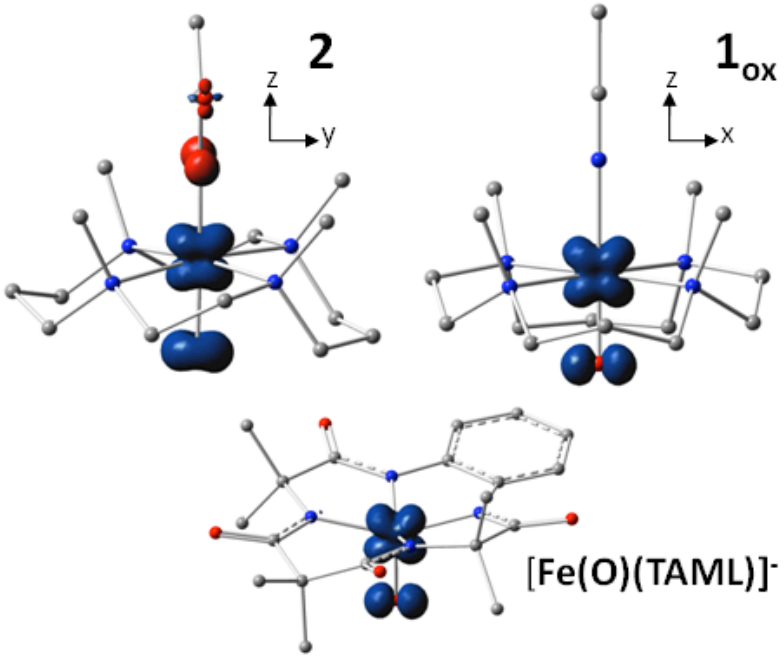

Figure S2. Spin density contour plots obtained with BP86/6-311G for three low-spin Fe^{V}-oxo complexes: complex **2**, ***1***$_{ox}$ (the computational model for the 1e-oxidized starting material), and the truncated TAML complex $[Fe^{V}(O)B^{*}]^{1-}$ (Tiago de Oliveira F, Chanda A, Banerjee D, Shan X, Mondal S, Que L, Jr., Bominaar EL, Münck E, & Collins TJ (2007) *Science* 315: 835-838) all viewed approximately along the normal to the plane containing the unpaired electron containing orbital, labeled d_{yz} (**2**) and d_{xz} (***1***$_{ox}$).

The spin density profiles shown in **Figure S2** corroborate the classification of **2** as an Fe^{V} complex. The spin density at the Fe=O moiety in **2** resembles the spin densities for the only Fe^{V}=O species, $[Fe^{V}(O)B^{*}]^{1-}$, reported in the literature and the computational model ***1***$_{ox}$, which is an Fe^{V} species as all ligands therein (MeCN, O^{2-}, TMC) are redox innocent. The p_y like contour of the spin density at the oxo atom in **2** is slightly blurred by the presence of some spin density in the p_x orbital of oxygen (**Table S7**) donated by the redox non-innocent imido nitrogen.

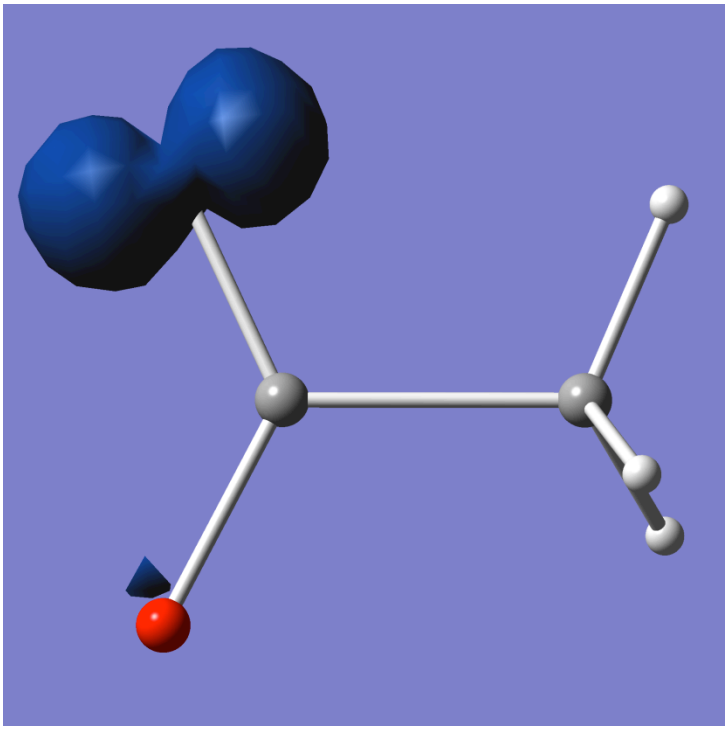

Figure S3. Plot of spin density in acetamidyl radical obtained with BP86 revealing the contour of the in-plane p orbital at nitrogen (labeled p_x in text) containing the unpaired electron.

BP86 optimized structure for **2**

Fe	-0.01024099	0.02306683	-0.09676283
N	-1.17725984	1.79683954	-0.25838780
N	1.70147703	1.32326218	-0.18781458
N	1.24788782	-1.71937391	-0.17896251
N	-1.64958483	-1.32346469	-0.24927041
C	-0.22538889	2.73632556	-0.97653287
C	1.13350707	2.73295991	-0.31166926
C	2.48552484	0.96919266	-1.44510015
C	3.07159865	-0.45288621	-1.47149840
C	2.07292973	-1.62287157	-1.45261501
C	0.28028651	-2.89566926	-0.25109017
C	-1.01205607	-2.51712182	-0.94027235
C	-2.76092048	-0.83353673	-1.16064998
C	-3.34520464	0.52456157	-0.77642209
C	-2.40708660	1.67341700	-1.13985877
C	-1.58273952	2.36561082	1.07472857
C	2.62601819	1.36498493	1.00369954
C	2.16058930	-2.03551189	0.98720274
C	-2.25119711	-1.74304869	1.07040823
H	-0.64901529	3.75636444	-0.98310138
H	-0.15325115	2.37603244	-2.00869548
H	1.07409387	3.14835530	0.70297737
H	1.84284066	3.36092941	-0.87742810
H	3.30982356	1.70088430	-1.53684436

H	1.79575591	1.09343972	-2.28797093
H	3.62612662	-0.53472721	-2.42252407
H	3.83661553	-0.57935295	-0.68975147
H	1.37167123	-1.52058717	-2.28818943
H	2.62929944	-2.57272642	-1.55665785
H	0.77041764	-3.73378275	-0.77507854
H	0.09247804	-3.21006711	0.78296390
H	-1.71780112	-3.36580370	-0.92541474
H	-0.83344712	-2.22055315	-1.97982802
H	-3.54785643	-1.60885145	-1.15914278
H	-2.33529388	-0.76765408	-2.16975299
H	-3.65775398	0.55880825	0.27853673
H	-4.27102476	0.66305761	-1.35970031
H	-2.04204242	1.52149903	-2.16375698
H	-2.93898896	2.64111024	-1.09937846
H	-2.08639165	3.33644700	0.93151582
H	-0.70549037	2.49358628	1.71302746
H	-2.26000378	1.67043351	1.57900361
H	3.28452376	2.24613677	0.92733861
H	3.25159157	0.47389949	1.04727787
H	2.02571361	1.41831227	1.91660690
H	2.65615123	-3.00186872	0.79084278
H	1.56477083	-2.10515680	1.90413999
H	2.93049962	-1.27450408	1.10624736
H	-3.03126389	-2.50110729	0.88808564
H	-2.70216168	-0.87290256	1.55769434
H	-1.48497279	-2.13666742	1.74613582
C	-0.01203733	-0.39560906	2.96186581
N	0.00000000	0.00000000	1.68375635
C	-0.03346059	0.59798308	4.10178657
H	0.82068506	0.40332148	4.76743487
H	0.00593297	1.64220747	3.76336590
H	-0.94658200	0.45121239	4.69844472
O	0.00000000	-1.67578230	3.21192172
O	-0.05858361	0.01033995	-1.79669894

Comments on EPR and Mössbauer Spectra

In the following we add some details of the Mössbauer and EPR spectra we recorded. The appropriate comments are given in the captions of the figures. In the caption of Figure 3 we indicated that the sample for **2-H**$^+$ contains a 30% high-spin Fe^{III} contaminant. The 8.0 T spectrum of **Figure S4** proves this assertion. The spectrum also shows that A_x and A_y of **2** are negative. The magnitude of A_z of **2** and **2-H**$^+$ is small and we could not determine its sign.

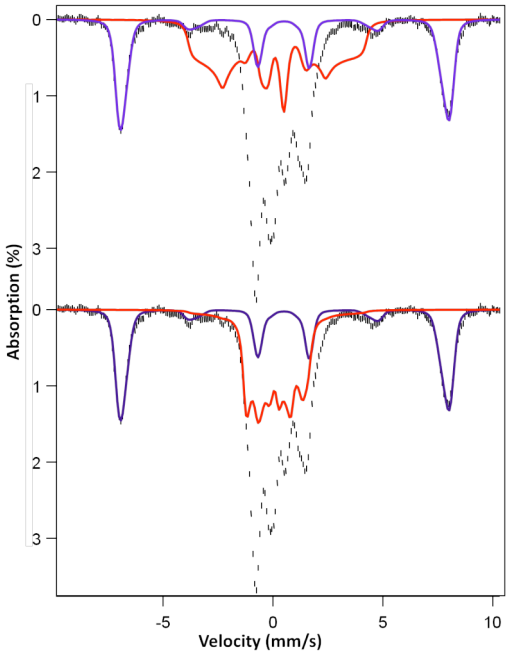

Figure S4. 4.2 K/8.0 T Mössbauer spectrum of the sample containing **2-H**$^+$ (Sample from Figure 3C). The purple line is a spectral simulation outlining the high-spin Fe^{III} contaminant (30% of Fe). The EPR spectra of this sample shows two high-spin Fe^{III} species with a positive zero-field splitting parameter D, $|D| < 2$ cm^{-1}, and E/D = 0.04 and 0.05. The red line in the bottom panel is a spectral simulation for **2-H**$^+$ assuming that A_x and A_y of **2** are **negative**. As shown in top panel, positive A_x and A_y values do not fit the data. A_z is too small, $|A_z| < 5$ MHz to determine its sign.

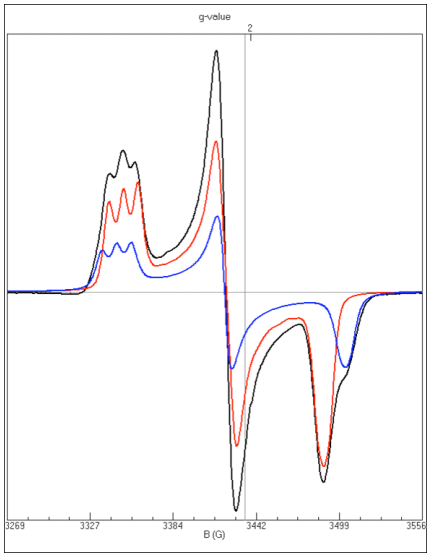

Figure S5. The black line shows a 40 K spectrum of **2** (same spectrum as shown in Figure 4A of the main text). The red line is a SpinCount simulation of the majority species, **2**. For the simulation the concentration of **2** was chosen to fit its high-field feature. It can be seen that this simulation does not produce sufficient amplitude for the low-field and middle resonances. The difference must be contributed by minority species $\mathbf{2^m}$ (blue line). Thus, the g-values of $\mathbf{2}^{m}$ are essentially known. $\mathbf{2}^{m}$ must also exhibit a ^{14}N hyperfine triplet, otherwise its low field feature would show a strong central peak due to the non-split line. Species $\mathbf{2}^{m}$ must be quite similar to **2**, but presently we do not know the conformational difference between the species (possibly different orientations of the imido ligand). Protonation always yields only one species $\mathbf{2\text{-}H}^{+}$. There is no hint in our data indicating that the Mössbauer spectra of **2** and $\mathbf{2\text{-}H}^{+}$ differ.

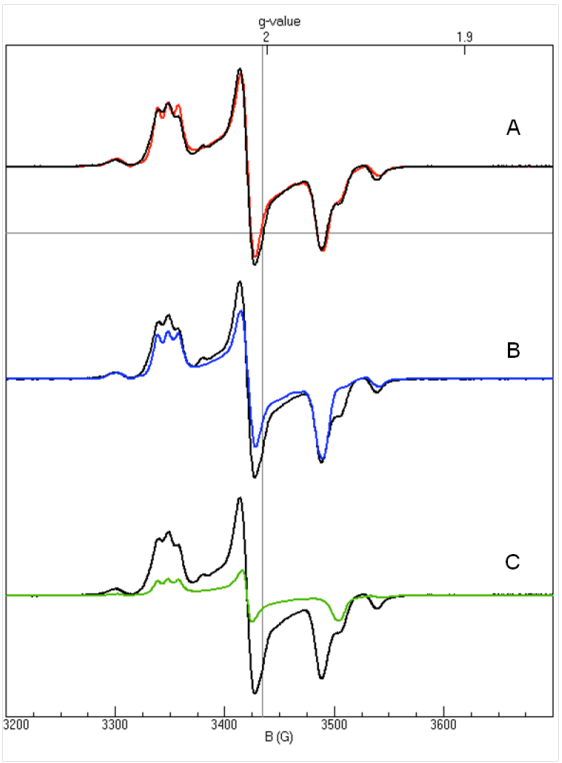

Figure S6. X-band EPR spectrum of ^{17}O labeled 2 (black lines) obtained in 3:1 PrCN:MeCN at 40 K. (A) SpinCount simulations of 2 and 2^{m} added in 2:1 ratio (red line). In (B) and (C) are shown the individual simulations of for 2 (blue) and 2^{m} (green) separately, in 2:1 proportions. Parameters used for 2 and 2^{m} (italics): $g_{x,y,z}$ =2.054, 2.010, 1.971 (*2.054, 2.011, 1.963*); $A_{x,y,z,}$(^{14}N, MHz) = 28.5, 10.5, 12 (*28.5, 2.6, 11)*, $A_{x,y,z,}$ (^{17}O, MHz) = 30, 130, 20 (*30, 130, 20)*, Lorentzian line width = 4 gauss.

Comments on Resonance Raman Data.

As ^{18}O labeling of **2** yielded two features centered at 762.5 cm^{-1}, we conducted additional labeling experiments to determine if these vibrations could be attributed to a Fermi doublet. Preparation of **2** using $PhI^{18}O$ to ensure that only one ^{18}O atom was incorporated into the final product also yielded the previously observed doublet, while generation of **2** using ^{17}O produced a single resonance-enhanced vibrational feature at 780 cm^{-1}. Thus, the pair of features at 762.5 cm^{-1} can be conclusively assigned as a Fermi doublet.

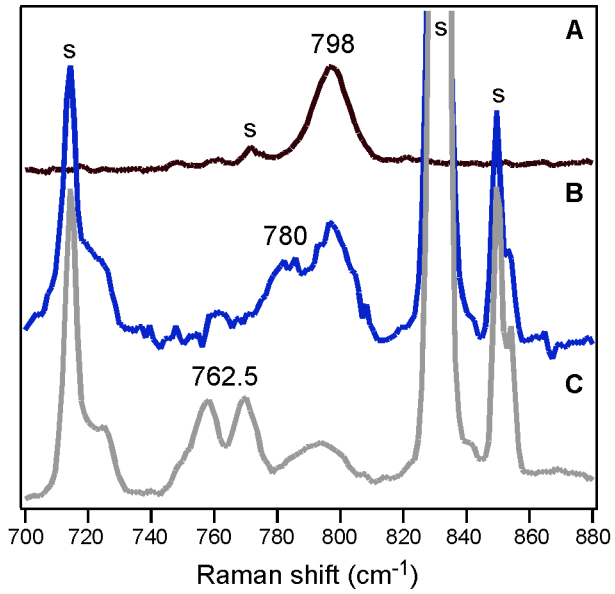

Figure S7. (A) rR spectrum of **2** in frozen CH_3CN. (B) rR spectra of ^{17}O-labeled **2** in CD_3CN. This sample was prepared by treating **1** with 100 equivalents of 60:40 $H_2{}^{16}O$:$H_2{}^{17}O$ at RT for 10 minutes, followed by addition of TBHP and base at -44 °C. (C) rR spectra of ^{18}O-labeled **2** prepared with solid $PhI^{18}O$ in CD_3CN. A small amount of unlabeled complex is also evident at ~798 cm^{-1}. All spectra were obtained with 457.9 nm laser excitation (~100 mW at source). S = solvent-derived peaks.

Comments on Low-temperature ESI-MS Experiments.

The use of the solvent mixture 3:1 CH_2Cl_2:CH_3CN allowed us to cool our system to -80°C and thus sufficiently stabilize **2** to conduct low-temperature ESI-MS experiments. The reaction vessel was immersed in dry ice, and a 0.4 mM solution of **2** was infused directly into the Bruker BioTOFFII in order to minimize sample decay. Parallel samples were prepared, one using 3:1 CH_2Cl_2:CH_3CN and the other 3:1 CH_2Cl_2:CD_3CN (Figure S8). Consistent with the results of Mössbauer analysis, ESI-MS investigations reveal a distribution of species (Figure S9).

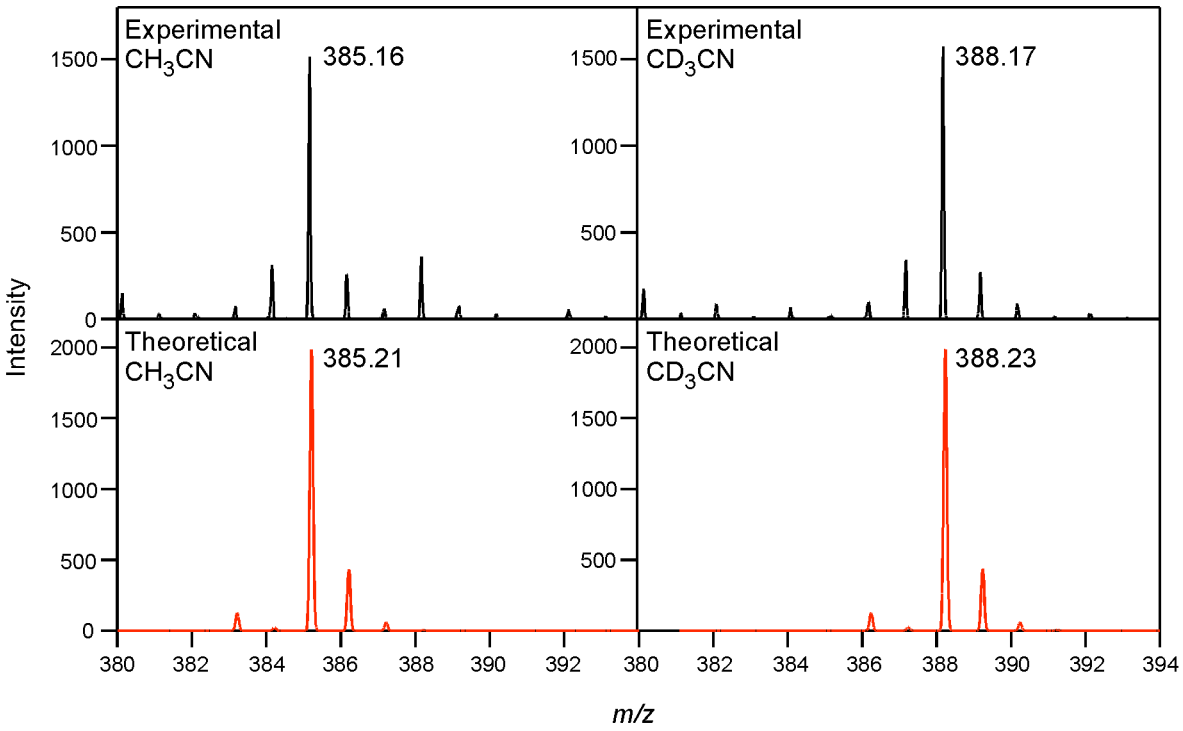

Figure S8. The electrospray ionization mass spectra (ESI-MS) of samples of **2** prepared in (left) 3:1 CH_2Cl_2:CH_3CN and (right) 3:1 CH_2Cl_2:CD_3CN. The theoretical spectra correspond to the expected isotope patterns of the cation $[Fe(O)(TMC)(NCOCH/D_3)]^+$.

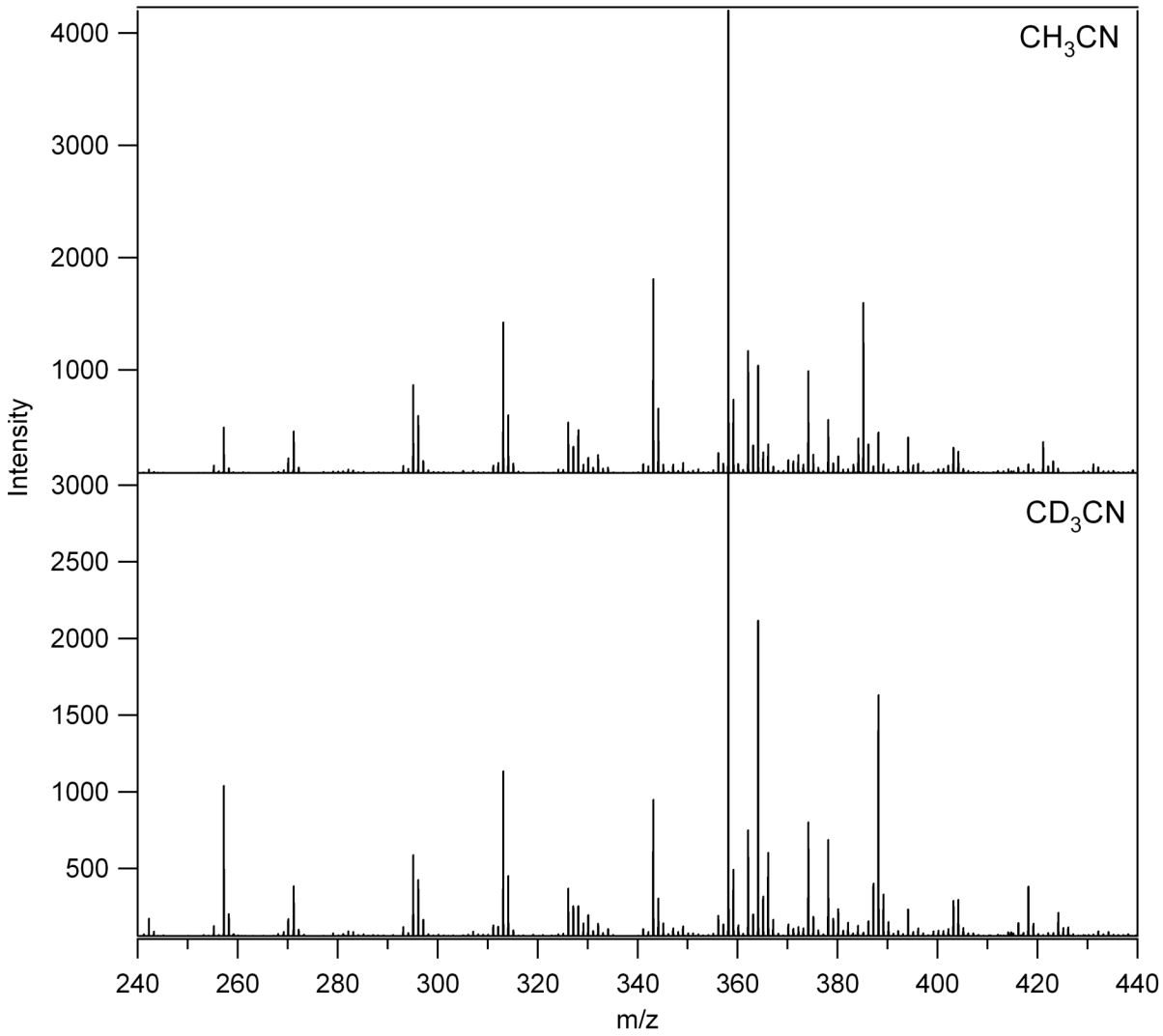

Figure S9. The electrospray ionization mass spectra (ESI-MS) of samples of **2** prepared in (top) 3:1 CH_2Cl_2:CH_3CN and (bottom) 3:1 CH_2Cl_2:CD_3CN.